# A Sensor Topology for Noncontact AC Voltage Measurement of Polyphase Cables

Thomas C. Krause, *Graduate Student Member, IEEE*, Katherine Camenzind, Daisy H. Green, *Graduate Student Member, IEEE*, Andrew Moeller, Łukasz Huchel, and Steven B. Leeb, *Fellow, IEEE*

***Abstract*— This article presents a sensor topology and signal processing technique for noncontact measurement of polyphase line-to-line voltage. Conductive plates around the exterior of a three-phase cable form a circuit that can be used to disaggregate the ac voltages in the cable. Fully differential transimpedance amplifiers detect capacitive currents that can be related mathematically to line-to-line voltages. Sensor calibration and line-to-line voltage reconstruction results are presented.**

***Index Terms*— Capacitive sensing, digital signal processing, load monitoring, power monitoring, sensor systems and applications.**

## I. Introduction

SOPHISTICATED systems for control, consumption score-keeping, and fault detection and diagnostics require access to system variables, such as voltage, current, and fluid flow. Noncontact sensors permit measurement of these system variables with inherent isolation and a reduced installation effort [1]. However, noninvasive or noncontact schemes for instrumentation and measurement frequently require signal processing and careful management of unintended or unavoidable cross coupling to ensure accurate estimation. These extra burdens limit situations in which noncontact sensing can be applied.

For example, noncontact ac voltage measurement for single-phase applications has been investigated [2], [3]. One solution uses a differential pickup to reject common-mode fields and to therefore provide more accurate voltage reconstruction [1], [4]. In [5]–[7], a reference plate driven with a sinusoidal voltage is used to determine the capacitance between the sensing plate and the conductor of interest. This method can adjust to capacitance variations and leads to very precise voltage reconstruction. Unfortunately, this technique does not scale to polyphase systems without intrusive separation of the cable and measurement of each separate wire.

Manuscript received August 25, 2021; revised September 30, 2021; accepted October 23, 2021. Date of publication November 16, 2021; date of current version February 21, 2022. This work was supported in part by the Grainger Foundation and in part by the Exelon Corporation through the MIT Energy Initiative. The Associate Editor coordinating the review process was Dr. He Wen. *(Corresponding author: Thomas C. Krause.)*

Thomas C. Krause, Daisy H. Green, Andrew Moeller, and Steven B. Leeb are with the Department of Electrical Engineering and Computer Science, Massachusetts Institute of Technology, Cambridge, MA 02139 USA (e-mail: tkrause@mit.edu; dhgreen@mit.edu; amoeller@mit.edu; sbleeb@mit.edu).

Katherine Camenzind and Łukasz Huchel are with the MIT Grainger Energy Machines Facility, Cambridge, MA 02139 USA.

Digital Object Identifier 10.1109/TIM.2021.3128709

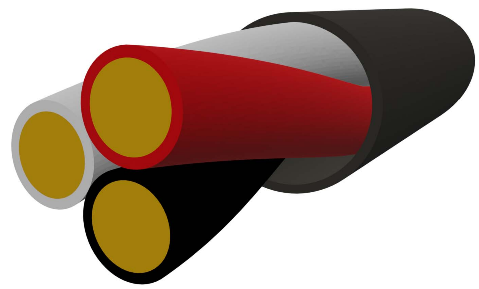

Fig. 1. Model of a three-wire power cable.

For polyphase systems, noncontact ac voltage measurement of overhead high-voltage transmission lines has been studied. The sensing plates and their resultant capacitances are often referred to as "open-air sensors" or "air capacitors" [8]–[10], with the inevitable problem of cross coupling between sensing plates and phase voltages. Three techniques for capacitance matrix estimation and sensor calibration are investigated in [11]. These techniques are applied to separated overhead wires with physically distant sensing instrumentation. These techniques depend on significant physical separation and are not easily extended to closer geometries of interest, notably multiconductor cables.

In this article, a sensor topology and signal processing technique for noncontact ac voltage measurement of polyphase cables is presented. The proposed measurement system extends noncontact ac voltage measurement to multiconductor cables. A three-phase system is investigated as an industrially relevant example, but the techniques developed in this article can be applied to cables and situations with more than three wires and more than three phases. For demonstration, a "delta connected" sensor topology is used to probe a three-phase cable. Simulation and experimental results characterize and verify the performance of the noncontact sensor.

## II. System Geometry and Capacitance

In this section, the term "wire" is used to refer to a conductor, stranded or unstranded, and the insulation that surrounds that conductor. The term "cable" refers to a group of wires and the surrounding insulation, shielding, armoring, or other material. For example, Fig. 1 shows a three-wire

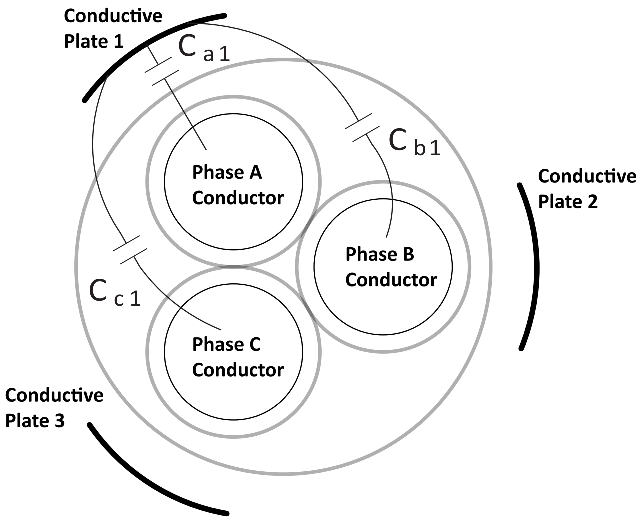


Fig. 2. Cross section of a three-wire power cable and three external conductive plates.

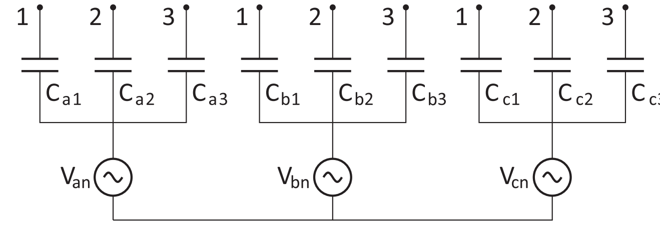


Fig. 3. Electrical schematic representation of the cable and plate system.

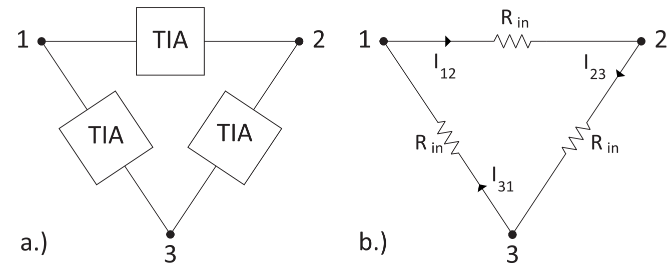


Fig. 4. Delta-connected sensor. (a) Sensor with TIA blocks. (b) Sensor model with input impedances of the TIAs.

power cable. Polyphase power cables are separated into three classes: low voltage (under 1 kV), medium voltage (2–35 kV), and high voltage (above 35 kV) [12]. The intended application determines cable characteristics, such as wire count, armoring, shielding, and insulation. For example, shielded cables are used for high-voltage systems [13], [14]. Capacitive sensing is challenging for shielded cables because the electric fields generated by the internal conductors terminate on the shield. This article presents capacitive noncontact ac voltage measurement for unshielded low-voltage power cables.

A capacitance exists between any two conductors. Linear capacitance is defined as the ratio of the absolute value of the charge on each conductor, $Q$, and the absolute value of the potential difference between the conductors, $V$ [15]. The capacitance between any two conductors is therefore determined by the conductor geometry and the material properties of their surrounding medium. Wire count, conductor size, and insulation thickness dictate power cable geometry. Unshielded low-voltage three-phase power cables are available in three-, four-, and five-wire configurations. In this article, power cables with three wires are considered as an example; however, the techniques described herein are applicable to three-, four-, or five-wire cables and other polyphase configurations.

A cross section of a three-phase power cable and three external conductive sensing plates is shown in Fig. 2. The capacitances between the wires and plate 1 are illustrated. Similar wire-to-plate capacitances exist for plates 2 and 3. To establish consistent notation for the capacitances of interest, in this article, wire-to-plate capacitances are denoted with the subscript of the wire phase assignment followed by the plate number, e.g., the capacitance from the phase a wire to plate 1 is denoted as $C_{a1}$. The plates in Fig. 2 are spaced by 120° and each positioned over a wire such that the capacitance to the underlying wire is maximized. In this analysis, the maximized capacitances, that is, $C_{a1}$, $C_{b2}$, and $C_{c3}$, are referred to as "primary capacitances." All other wire-to-plate capacitances are referred to as "secondary capacitances."

A schematic of the cable and plate system is shown in Fig. 3. Nodes 1–3 are the conductive plates of Fig. 2. Note that the wire-to-wire and plate-to-plate capacitances are neglected as symmetry makes them essentially irrelevant for voltage estimation. This schematic suggests the application of a "delta-connected" sensor circuit topology, as shown in Fig. 4. Each branch of the sensor circuit is a fully differential transimpedance amplifier (TIA), as shown in Fig. 4(a). The amplifiers present identical input impedance, $R_{\text{in}}$, shown in Fig. 4(b). The fully differential TIAs convert branch currents into differential voltage signals. The circuit analysis of this sensor topology is discussed in Section III.

## III. Circuit Analysis

In this section, "$s$-domain" (Laplace transform) expressions for the branch currents of the noncontact sensor are derived. A nodal analysis is used to build a system of equations. Node voltages are determined and interpreted. The results emphasize the importance of the system geometry.

The circuit comprised of Figs. 3 and 4(b) is considered. Kirchoff's current law (KCL) evaluated at nodes 1–3, with positive currents defined as flowing into the node, leads to the following equations:

$$\begin{aligned} I_{C_{a1}}(s) + I_{C_{b1}}(s) + I_{C_{c1}}(s) + I_{31}(s) - I_{12}(s) &= 0 \\ I_{C_{a2}}(s) + I_{C_{b2}}(s) + I_{C_{c2}}(s) + I_{12}(s) - I_{23}(s) &= 0 \\ I_{C_{a3}}(s) + I_{C_{b3}}(s) + I_{C_{c3}}(s) + I_{23}(s) - I_{31}(s) &= 0 \end{aligned} \tag{1}$$

where $I_{C_{xx}}(s)$ are capacitor currents and $I_{xx}(s)$ are sensor circuit branch currents as defined in Fig. 4(b). Each current in (1) is expressed in terms of the node voltages using Ohm's law. For example, the current through capacitor $C_{a1}$ is

$$I_{C_{a1}}(s) = \frac{V_{an}(s) - V_1(s)}{\frac{1}{sC_{a1}}}. \tag{2}$$

Each current is rewritten and (1), expressed in a matrix form, becomes

$$\boldsymbol{A}(s)\boldsymbol{X}(s) = \boldsymbol{B}(s) \tag{3}$$

where the system (conductance) matrix, $\boldsymbol{A}(s)$, is

$$\boldsymbol{A}(s) = \begin{bmatrix} A_{11}(s) & A_{12}(s) & A_{13}(s) \\ A_{21}(s) & A_{22}(s) & A_{23}(s) \\ A_{31}(s) & A_{32}(s) & A_{33}(s) \end{bmatrix} \tag{4}$$

the diagonal terms are

$$\begin{aligned} A_{11}(s) &= s(C_{a1} + C_{b1} + C_{c1}) + \frac{2}{R_{\text{in}}} \\ A_{22}(s) &= s(C_{a2} + C_{b2} + C_{c2}) + \frac{2}{R_{\text{in}}} \\ A_{33}(s) &= s(C_{a3} + C_{b3} + C_{c3}) + \frac{2}{R_{\text{in}}} \end{aligned} \tag{5}$$

the off-diagonal terms are

$$\begin{aligned} &A_{21}(s) = A_{31}(s) = A_{32}(s) = \\ &A_{12}(s) = A_{13}(s) = A_{23}(s) = \frac{-1}{R_{\text{in}}}, \end{aligned} \tag{6}$$

the node voltage vector, $\boldsymbol{X}(s)$, is

$$\boldsymbol{X}(s) = \begin{bmatrix} V_1(s) \\ V_2(s) \\ V_3(s) \end{bmatrix} \tag{7}$$

and the source vector, $\boldsymbol{B}(s)$, is

$$\boldsymbol{B}(s) = \begin{bmatrix} s(C_{a1}V_{an}(s) + C_{b1}V_{bn}(s) + C_{c1}V_{cn}(s)) \\ s(C_{a2}V_{an}(s) + C_{b2}V_{bn}(s) + C_{c2}V_{cn}(s)) \\ s(C_{a3}V_{an}(s) + C_{b3}V_{bn}(s) + C_{c3}V_{cn}(s)) \end{bmatrix}. \tag{8}$$

All circuit parameters of (3) and the Laplace variable, $s$, are defined as symbolic variables and the MATLAB Symbolic Toolbox [16] is used to solve the system, (3), for $\boldsymbol{X}(s)$. From that result, the branch currents are known, e.g.,

$$I_{12}(s) = \frac{V_1(s) - V_2(s)}{R_{\text{in}}} \tag{9}$$

where the node voltages are functions of the passive components, the Laplace variable, and the line-to-neutral voltages. The line-to-neutral voltages can be rewritten in terms of the line-to-line voltages. These substitutions yield a relationship between the branch currents and the line-to-line voltages described by a transfer function matrix, $\boldsymbol{H}(s)$

$$\begin{bmatrix} I_{12}(s) \\ I_{23}(s) \\ I_{31}(s) \end{bmatrix} = \begin{bmatrix} H_{11}(s) & H_{12}(s) & H_{13}(s) \\ H_{21}(s) & H_{22}(s) & H_{23}(s) \\ H_{31}(s) & H_{32}(s) & H_{33}(s) \end{bmatrix} \begin{bmatrix} V_{ab}(s) \\ V_{bc}(s) \\ V_{ca}(s) \end{bmatrix}. \tag{10}$$

The terms of $\boldsymbol{H}(s)$ are functions of the wire-to-plate capacitances, $C_{xx}$, the input impedance of the TIAs, $R_{\text{in}}$, and the Laplace variable, $s$. Unfortunately, the terms of $\boldsymbol{H}(s)$ are too big to present satisfactorily. The following substitutions for the wire-to-plate capacitances simplify the terms of $\boldsymbol{H}(s)$:

$$\begin{aligned} &\begin{bmatrix} C_{a1} & C_{a2} & C_{a3} \\ C_{b1} & C_{b2} & C_{b3} \\ C_{c1} & C_{c2} & C_{c3} \end{bmatrix} \\ &\quad = \begin{bmatrix} C_p + \Delta C_{a1} & C_s + \Delta C_{a2} & C_s + \Delta C_{a3} \\ C_s + \Delta C_{b1} & C_p + \Delta C_{b2} & C_s + \Delta C_{b3} \\ C_s + \Delta C_{c1} & C_s + \Delta C_{c2} & C_p + \Delta C_{c3} \end{bmatrix} \end{aligned} \tag{11}$$

where $C_p$ is the common component of the primary capacitances, $C_s$ is the common component of the secondary capacitances, and $\Delta C_{xx}$ are imbalance capacitances. If all capacitances are balanced, that is, all imbalance capacitances $\Delta C_{xx} = 0$, then $\boldsymbol{H}(s)$ is a diagonal matrix. Simplified symbolic expressions for the imbalanced case are given in the Appendix. In the balanced case, the diagonal terms are

$$H_{11}(s) = H_{22}(s) = H_{33}(s) = \frac{(C_p - C_s)s}{(C_p + 2C_s)R_{\text{in}}s + 3}. \tag{12}$$

The balanced case is the motivation for the proposed sensor topology. For most applications, the capacitances $C_p$ and $C_s$ are on the order of picofarads such that $(C_p + 2C_s)R_{\text{in}}s \ll 3$ and the transfer function in (12) simplifies to $(1/3)(C_p - C_s)s$. In this scenario, the branch currents in the sensor circuit are scaled versions of the derivatives of the line-to-line voltages in the cable.

This analysis motivates the development of a "delta-connected" sensor topology that measures the branch currents between conductive sensing plates. Balanced primary and secondary wire-to-plate capacitances lead to an advantageous cancellation of terms. A specific circuit realization comprised of fully differential TIAs is presented in Section IV.

## IV. Sensor Topology

A sensor with three branch current sensing channels is presented in this section. Each channel outputs a single-ended voltage to interface easily with data acquisition units (DAQs). For this application, an analog front end comprised of fully differential TIAs is used to sense the branch currents. Fully differential TIAs have documented use in capacitive sensing applications [17]–[19].

### A. Fully Differential Amplifier

For in-depth derivations and application examples of fully differential amplifiers, see [20] and [21]. Fully differential amplifiers utilize differential signaling for both the input and the output. The common-mode output, $V_{\text{oc}}$, is adjustable via a pin, $V_{\text{ocm}}$. A separate common-mode output voltage amplifier and feedback loop ensure proper regulation. A modeling approach for fully differential amplifiers with imbalanced feedback impedances is given in [22]. The analysis presented below assumes well-matched feedback paths and mirrors the analysis mentioned in [20].

A fully differential amplifier is shown in Fig. 5. The differential action of the amplifier is characterized by

$$(V_{\text{out}}+) - (V_{\text{out}}-) = A_{\text{ol}}(V_p - V_n) \tag{13}$$

where $A_{\text{ol}}$ is the differential open-loop gain of the amplifier. The common-mode output voltage definition, $V_{\text{oc}}$, is

$$V_{\text{ocm}} = V_{\text{oc}} = \frac{((V_{\text{out}}+) + (V_{\text{out}}-))}{2}. \tag{14}$$

After some work, circuit analysis and (13) and (14) yield a relationship between $V_{\text{in}}+$, $V_{\text{in}}-$, $V_{\text{out}}+$, $V_{\text{out}}-$, and circuit parameters

$$\frac{(V_{\text{out}}+) - (V_{\text{out}}-)}{(V_{\text{in}}+) - (V_{\text{in}}-)} = \frac{V_{\text{od}}}{V_{\text{id}}} = \frac{1-\beta}{\beta\left(1 + \frac{1}{A_{\text{ol}}\beta}\right)} \tag{15}$$

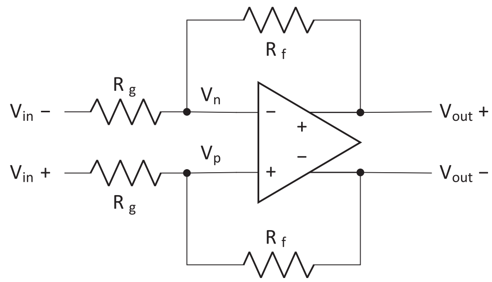


Fig. 5. Fully differential amplifier with symmetric feedback paths.

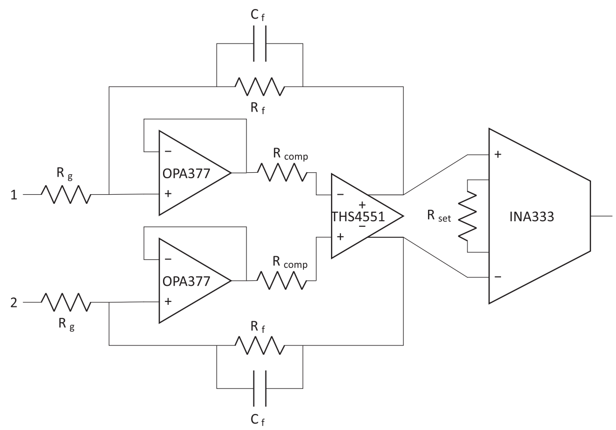


Fig. 6. Schematic of one TIA channel.

where $\beta = R_g/(R_g + R_f)$. The open-loop differential gain is assumed to be very large, i.e., $A_{\mathrm{ol}}\beta \gg 1$, and with $\beta$ written out, (15) simplifies to

$$\frac{V_{\mathrm{od}}}{V_{\mathrm{id}}} = \frac{R_f}{R_g}. \tag{16}$$

TIAs sense a current signal and produce a corresponding voltage signal; therefore, TIAs have a gain with units of ohms, and the output voltage is divided by input current. To yield a fully differential TIA gain expression, the input impedance of Fig. 5 and (16) is considered. Equation (13) suggests that $V_p = V_n$ if $A_{\mathrm{ol}} \gg 1$, known as the "virtual short circuit" assumption. Under this assumption, the input impedance of the fully differential amplifier is equal to $2R_g$. For an input voltage $V_{\mathrm{id}}$, a current $I_{\mathrm{in}} = (V_{\mathrm{id}}/2R_g)$ will flow between the terminals. Equation (16), with $V_{\mathrm{id}}$ written in terms of $I_{\mathrm{in}}$, yields the TIA gain expression

$$\frac{V_{\mathrm{od}}}{I_{\mathrm{in}}} = 2R_f. \tag{17}$$

### B. Prototype Circuitry

A schematic of one channel of the realized sensor is shown in Fig. 6. The prototype employs the THS4551 fully differential amplifier [23]. An OPA377 CMOS operational amplifier is used in a unity-gain buffer configuration to limit the effect of input-bias current on the sensed signals. The OPA377 has a typical input-bias current of $\pm 0.2pA$ [24]. The instrumentation amplifier, INA333, is used to convert the differential output of the THS4551 into a single-ended voltage signal. The parallel feedback capacitor, $C_f$, is added to reduce gain at high frequencies. The resistor $R_{\mathrm{comp}}$ is a series compensation resistor that stabilizes the unity-gain buffer.

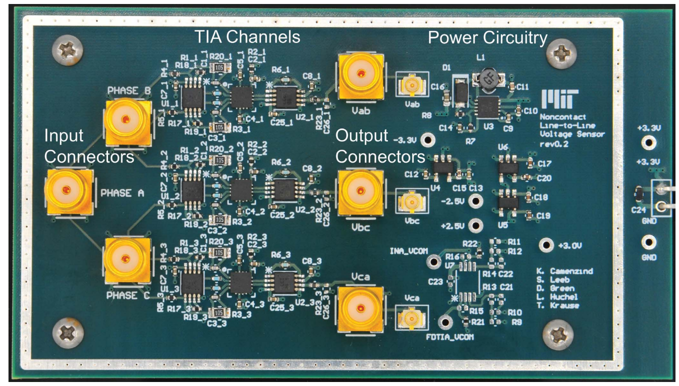


Fig. 7. Realized sensor.

TABLE I
REALIZED SENSOR COMPONENT VALUES

| Parameter | Value |
|---|---|
| Fully-Differential Amplifier | THS4551 |
| Unity-Gain Buffer | OPA377 |
| Instrumentation Amplifier | INA333 |
| $R_g$ | 100 kΩ |
| $R_f$ | 1 MΩ |
| $C_f$ | 3 pF |
| $R_{comp}$ | 21.5 kΩ |
| $R_{set}$ | 1.96 kΩ |

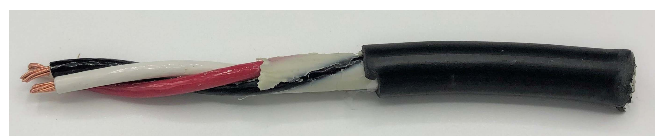

Fig. 8. Section of LSTSGU-4 cable.

The prototype sensor is shown in Fig. 7. The populated component values are given in Table I. The four-layer board accepts +3.3 V and ground connections through the two-pin connector located on the right edge of the board. Power circuitry generates ±2.5 V rails that power the analog circuitry. The input connections are located on the left side of the board. Input connections to the conductive plates use coaxial cable and Sub-Miniature version A (SMA) connectors for good shielding. The three TIA channels are located between the input and output connectors. The sensor outputs are available via SMA and U.FL connectors to interface simultaneously with an oscilloscope and DAQ.

## V. Cable Application

This section introduces a probe that realizes the conductive sensing plates. The noncontact sensor is paired with the probe and applied to a three-wire shipboard cable. A CAD model of the probe and cable is presented. Wire-to-plate capacitances are extracted from the CAD model. MATLAB

TABLE II
LSTSGU-4 SPECIFICATIONS

| Parameter | Value |
|---|---|
| Military Specification | M24643/16 |
| Nominal Cable O.D. (in) | 0.449 in |
| Number of Conductors | 3 |
| Conductor AWG | 14 AWG |
| Amps per Conductor | 17 A |
| Strands per Conductor | 7 |
| Insulation Material | Silicone Rubber |
| Jacket Material | Halogen-Free Cross-Linked Polyolefin |

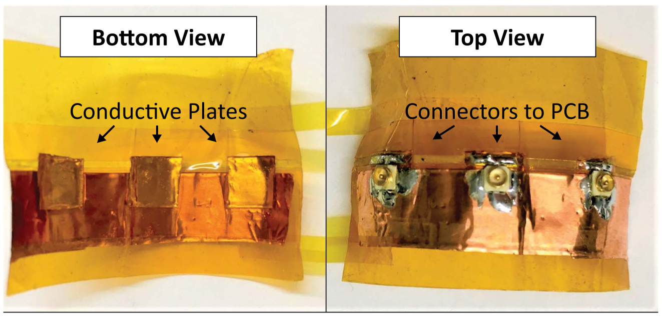


Fig. 9. Kapton and copper tape structure.

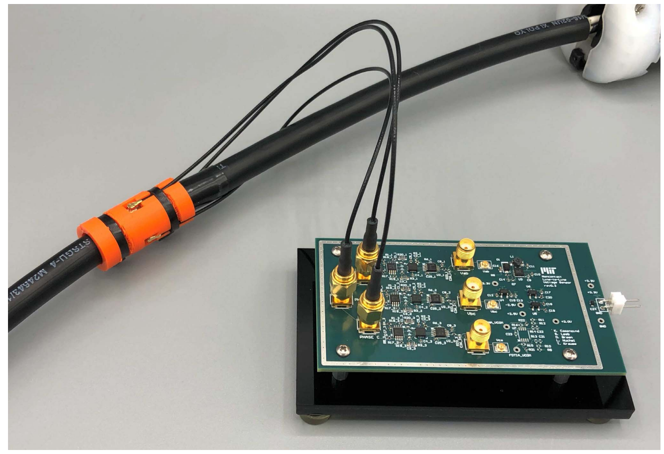

Fig. 10. Installed probe and sensor.

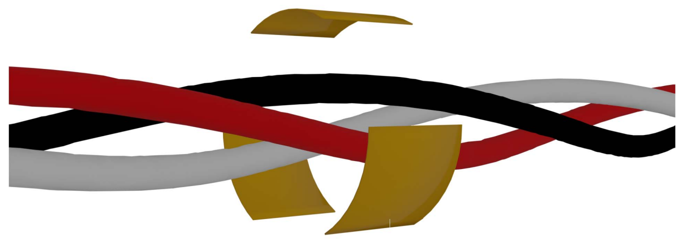

Fig. 11. FreeCAD solids used in the Fastercap simulation.

and SPICE simulations of the system are introduced and use the extracted capacitances. Simulation results are compared with experimental results. A calibration and reconstruction procedure is presented.

A section of LSTSGU-4 cable is shown in Fig. 8. Table II lists the specifications of the cable. The noncontact sensor requires a probe of conductive plates to capacitively couple to the cable wires. The core of the probe, shown in Fig. 9, is constructed with Kapton and copper tape. The bottom layer has three 6 mm × 6 mm pieces of copper tape spaced appropriately for the target cable. The top layer provides shielding and secures the U.FL connectors. A 3-D printed clamp completes the probe and provides a solid connection to the cable. Fig. 10 shows the probe installed on the LSTSGU-4 cable. Alignment of the probe plates over phase conductors was achieved through observation of the sensor outputs during probe installation. For a balanced set of cable voltages, a balanced set of sensor outputs indicates the correct probe location.

### A. Modeling

The probe plates and cable wire conductors are modeled in FreeCAD, rendered in Fig. 11. The model accounts for wire "twist" and uses a 60- mm pitch as estimated from the sample cable. The model plates match the physical dimensions of the real probe plates and are similarly placed over the phase conductors, that is, the plate placement of Fig. 2. A Python script developed by FastFieldSolvers converts the FreeCAD objects into input files readable by Fastercap, a capacitance extraction software [25], [26]. Fastercap computes the capacitances between all conductors. Dielectric materials are not included in the FreeCAD model, and therefore, the Fastercap results must be multiplied by the estimated relative permittivity of the surrounding medium. The jacket and insulation materials listed in Table II have the relative permittivities of 2.3 and 3.3, respectively [27]. A permittivity estimate of 2.5 represented the cable materials and the extracted capacitances are

$$\begin{bmatrix} C_{a1} & C_{a2} & C_{a3} \\ C_{b1} & C_{b2} & C_{b3} \\ C_{c1} & C_{c2} & C_{c3} \end{bmatrix} = \begin{bmatrix} 349\ \text{fF} & 115\ \text{fF} & 113\ \text{fF} \\ 114\ \text{fF} & 350\ \text{fF} & 113\ \text{fF} \\ 114\ \text{fF} & 115\ \text{fF} & 357\ \text{fF} \end{bmatrix}. \quad (18)$$

Two models are compared to experimental results. The first model is a MATLAB script that solves the system of Section III, (3), in sinusoidal steady state, i.e., phasor analysis ($s = jw$). The line-to-neutral voltages represent balanced sinusoidal 60- Hz, 120-$V_{\text{rms}}$ excitation. Expressed in phasor notation, the line-to-neutral voltages are $V_{an} = 120\underline{/0^\circ}$, $V_{bn} = 120\underline{/-120^\circ}$, and $V_{cn} = 120\underline{/120^\circ}$. The TIA circuits are assumed to present identical input impedances, $R_{\text{in}} = 2R_g$, where $R_g$ is equal to 100 kΩ in the realized sensor. The script solves for the node voltage vector, $\boldsymbol{X}(s)$, and uses Ohm's law to solve for the branch currents. The branch currents are multiplied by the ideal gain of the TIA channels to yield sensor outputs. The gain of a TIA channel is the product of the gain of the fully differential TIA and the gain of the instrumentation amplifier

$$\text{Gain} = (2R_f)\left(1 + \frac{100\ \text{k}\Omega}{R_{\text{set}}}\right) \quad (19)$$

where, for the realized sensor, $R_f$ is equal to 1 MΩ and $R_{\text{set}}$ is equal to 1.96 kΩ. The overall gain is approximately 104 MΩ.

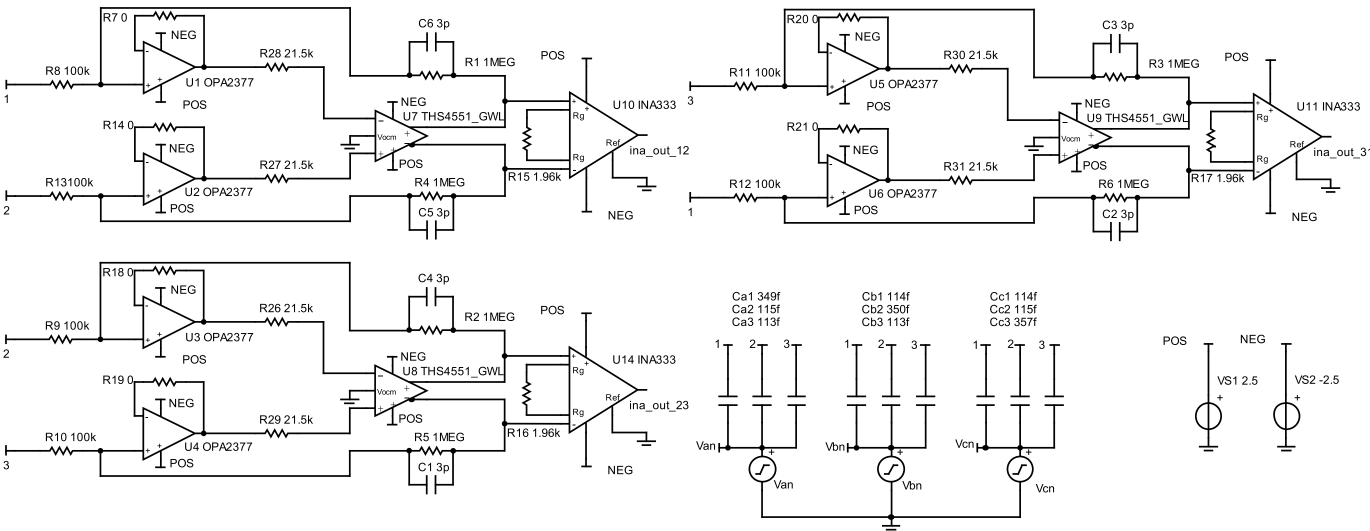


Fig. 12. TINA-TI schematic of the noncontact sensor.

TABLE III

SIMULATED AND EXPERIMENTAL SENSOR OUTPUTS FOR BALANCED 60-HZ, 120-$V_{rms}$ LINE-TO-NEUTRAL EXCITATION

| Method | Sensor Output | | |
|---|---|---|---|
| | Sensor Ch1 | Sensor Ch2 | Sensor Ch3 |
| MATLAB | 0.639 Vrms | 0.651 Vrms | 0.651 Vrms |
| SPICE | 0.636 Vrms | 0.648 Vrms | 0.648 Vrms |
| Experimental | 0.803 Vrms | 0.789 Vrms | 0.721 Vrms |

The second model, shown in Fig. 12, is a SPICE model built in TINA-TI. Component values match those populated on the realized sensor. The voltage sources are set to provide the balanced sinusoidal 60-Hz, 120-$V_{rms}$ excitation. An ac analysis is conducted to calculate the nodal voltages in a sinusoidal steady state.

The following experimental setup was used to validate the MATLAB and SPICE models. An Agilent 6834B AC Power Source provides sinusoidal three-phase voltage waveforms with controllable line-to-neutral magnitude and relative phase shift. The noncontact sensor interfaces with a custom six-channel power over Ethernet (PoE) DAQ. The DAQ provides +3.3V to power the noncontact sensor and simultaneously samples the sensor outputs. A personal computer communicates with the DAQ to initiate and download measurements. Measurements were further processed with Python or MATLAB scripts.

The simulation and experimental results are given in Table III. There is agreement between the MATLAB and SPICE simulations. The experimental results differ slightly from simulation, in part due to probe placement, permittivity differences, and deviations introduced by cable and probe construction. The results support and validate the sensor topology.

### *B. Calibration and Reconstruction Procedure*

Calibration of the noncontact sensor and the reconstruction process of the fundamental frequencies of the line-to-line voltages are presented. The three sensor outputs are scaled versions of the branch currents flowing in the sensor circuit between the sensing plates. For a well-placed probe and symmetric cable geometry, the branch currents are related to the line-to-line voltages through (12). Ideally, the sensor outputs could simply be integrated and scaled to reconstruct the line-to-line voltages. In practice, the relationships between the branch currents and the line-to-line voltages are influenced by the small but nonzero imbalance capacitances (see the Appendix). A more refined estimation procedure, therefore, integrates the sensor outputs and applies a scale factor and delay to the signals. The scale factors and delays are determined through calibration. Calibration requires a one-time accurate measurement of the line-to-line voltages provided by temporary contact measurement, for example, conductor-to-conductor contact with the phase wires through a three-phase plug. Calibration is necessary for each new installation of the sensor, that is, each new probe location.

The calibration procedure is shown in Fig. 13. The voltages are assumed to be in steady state during the calibration measurement time window. The window length is chosen to provide good frequency resolution after computation of the discrete Fourier transform (DFT). First, the noncontact sensor outputs are integrated. Lawrence *et al.* [4] have shown the benefits of digital integration in capacitive sensing applications. A Type 3 finite impulse response (FIR) filter presented in [4] is used to process the sensor outputs. The filter approximates integration and introduces 90° of phase lag at all frequencies. After integration, the contact and noncontact measurements follow similar paths. Both are low-pass filtered (LPF) to eliminate frequency components above the fundamental frequency, e.g., 60 Hz. To find the scale factor for corresponding signals, e.g., $V_{ab}$ and sensor channel 1, the maximum values of the DFTs are determined. The scale factor is equal to the peak DFT value of the contact measurement divided by the peak DFT value of the sensor output. To find the delay for the corresponding signals, the zero-crossing indices

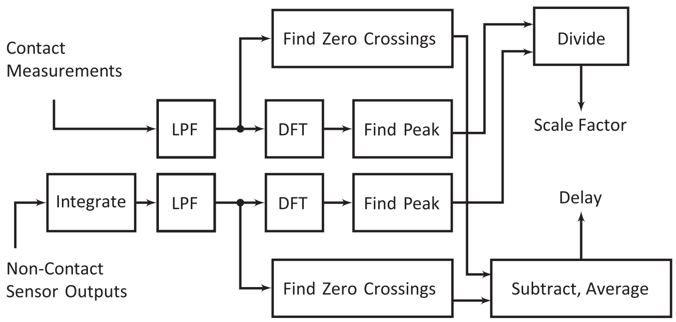


Fig. 13. Calibration procedure.

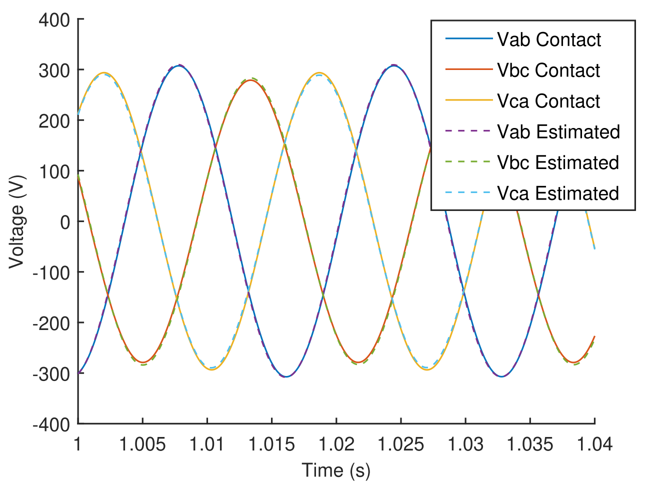


Fig. 14. Reconstruction for imbalanced Case 1 ($V_{an} = 132$ $\mathrm{V_{rms}}$, $V_{bn} = 120$ $\mathrm{V_{rms}}$, and $V_{cn} = 108$ $\mathrm{V_{rms}}$).

of the filtered time-domain waveforms are determined. The delay is equal to the index difference averaged across the measurement file. For systems with significant harmonic content, an extended calibration procedure with bandpass filters can be used. The bandpass filters isolate specific harmonics and their scale factors and delays can be determined via the same process outlined above. In this article, only the fundamental frequency is considered.

After calibration, the scale factors and delays are stored and the contact measurement system removed. To reconstruct, the integrated and LPF sensor outputs are scaled and shifted by their scale factor and delay, respectively. Perfect reconstruction is achieved for the calibration operating condition, i.e., the system voltages and probe placement for which the calibration parameters were calculated. Reconstruction error will arise for changes of the system voltages, however, these are reasonably small for a well-positioned probe.

## VI. Reconstruction Results

In this section, line-to-line voltage reconstruction from the noncontact sensor installed on the LSTSGU-4 shipboard cable is presented. LEM LV25-P voltage transducers provide contact voltage measurement and serve to calibrate and verify the noncontact sensor. The DAQ simultaneously samples the contact measurements and the noncontact sensor outputs. The sensor is calibrated with balanced three-phase 60- Hz, 120-$\mathrm{V_{rms}}$ excitation. In the first scenario, the steady-state performance of the sensor with imbalanced electrical system voltages is presented. In the second scenario, the transient performance of the sensor is presented.

TABLE IV
Voltage Reconstruction Results

| **Method** | $V_{ab}$ | $V_{bc}$ | $V_{ca}$ |
|---|---|---|---|
| | Case 1 | | |
| Contact | 216.86 Vrms | 196.92 Vrms | 207.27 Vrms |
| Non-Contact Sensor | 217.79 Vrms | 200.25 Vrms | 203.92 Vrms |
| Error | 0.43% | 1.69% | 1.61% |
| | Case 2 | | |
| Contact | 206.95 Vrms | 217.68 Vrms | 196.69 Vrms |
| Non-Contact Sensor | 204.12 Vrms | 219.61 Vrms | 199.10 Vrms |
| Error | 1.37% | 0.88% | 1.23% |
| | Case 3 | | |
| Contact | 196.25 Vrms | 207.66 Vrms | 217.47 Vrms |
| Non-Contact Sensor | 198.09 Vrms | 202.23 Vrms | 218.27 Vrms |
| Error | 0.94% | 2.61% | 0.37% |

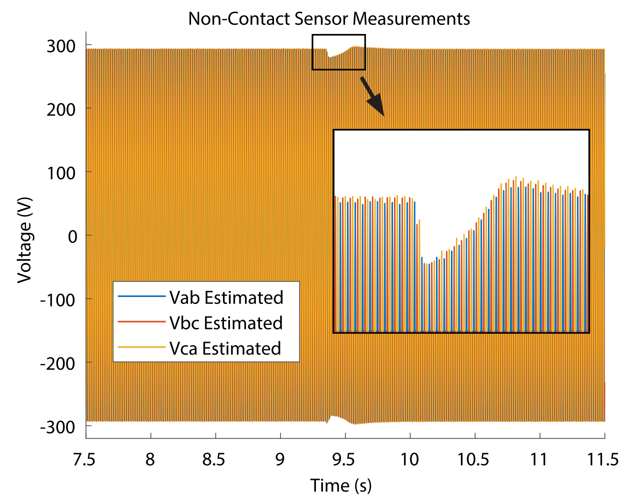


Fig. 15. Transient voltage distortion for induction motor turn-on.

### A. Steady-State Performance

To evaluate the performance of the noncontact sensor, the power source commands are varied and the line-to-line voltages are reconstructed. Three cases of imbalance are presented. In each case, two of the line-to-neutral voltages of the power source are given a 10% imbalance in opposite directions. For example, for Case 1, the line-to-neutral voltages are $V_{an} = 132$ $\mathrm{V_{rms}}$, $V_{bn} = 120$ $\mathrm{V_{rms}}$, and $V_{cn} = 108$ $\mathrm{V_{rms}}$. Contact line-to-line voltage measurements and reconstructed line-to-line voltage estimates from Case 1 are shown in Fig. 14. The contact measurements and voltage reconstruction results for all cases are presented in Table IV. The root-mean-square voltages are calculated from 5-s measurements of the

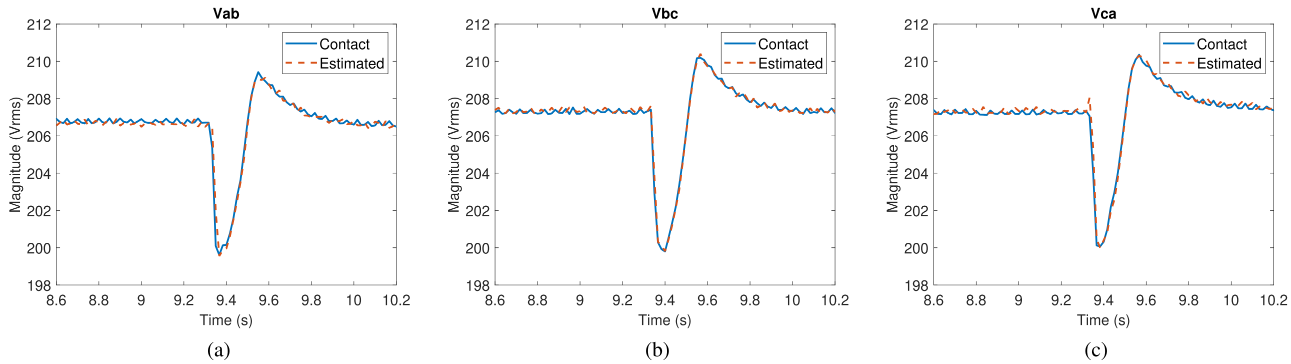


Fig. 16. Fundamental spectral envelopes of the system line-to-line voltages for induction motor turn-on. (a) $V_{ab}$. (b) $V_{bc}$. (c) $V_{ca}$.

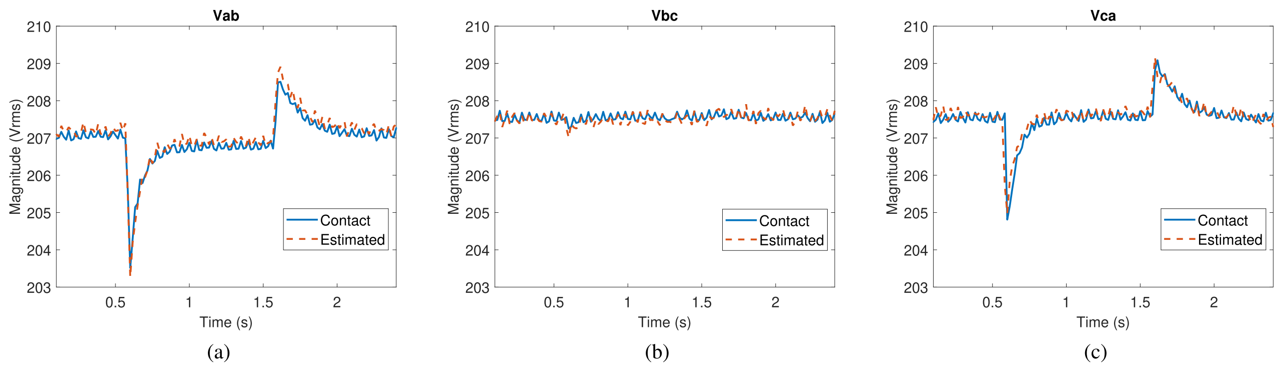


Fig. 17. Fundamental spectral envelopes of the system line-to-line voltages for lamp turn-on and turn-off. (a) $V_{ab}$. (b) $V_{bc}$. (c) $V_{ca}$.

calibrated sensor outputs. The noncontact sensor reconstructs the line-to-line voltages with small steady-state error compared to the imbalances applied to the system.

### *B. Voltage Transients*

Electrical system voltage regulators, for example, generator field winding exciters and diesel engine governors, have finite bandwidth. Consequently, for changes in electrical system load, voltage distortion events occur. Detection of these events is used for tracking power quality, load monitoring, and autonomous load coordination [28]–[30]. The calibrated noncontact sensor is used to track voltage during the transient events of a three-phase 180- W induction motor and a 250- W incandescent lamp. The lamp is a line-to-neutral load. A separate receptacle with connection to the Agilent 6834B AC Power Source neutral wire is broken out via extension cord and presents line-to-neutral connections for each phase.

The estimated line-to-line voltage measurements reconstructed from the noncontact sensor during induction motor startup are shown in Fig. 15. The voltage distortion during startup is highlighted. Power system voltage and current signals are often represented with spectral envelopes [29]–[31]. Spectral envelopes provide a measure of harmonic content averaged over every ac line cycle. The fundamental spectral envelopes of the voltages during the induction motor turn-on transient are shown in Fig. 16. The voltage estimates from the noncontact sensor match the reference contact measurements very well during the voltage distortion event.

The fundamental spectral envelopes of the voltages during the incandescent lamp turn-on (at $t = 0.5$ s) and turn-off (at $t = 1.5$ s) transients are shown in Fig. 17. The incandescent lamp is connected across phase a and neutral. Thus, voltage distortion appears on $V_{ab}$ and $V_{ca}$, but not $V_{bc}$. There is excellent agreement between the contact voltage measurements and the voltage estimates from the noncontact sensor.

## VII. Conclusion

In this article, a noncontact ac voltage sensor topology and signal processing technique for polyphase cables is presented. The operation of the sensor is described with circuit analysis. The analysis highlights the merits of the proposed topology. Two simulation models of the sensor are discussed. The MATLAB model and the SPICE model are verified with comparison to experimental results with a realized noncontact sensor. A sensor calibration and voltage reconstruction procedure is explained. The line-to-line voltages of an LSTSGU-4 three-phase shipboard cable are reconstructed with the prototype sensor. The noncontact sensor performs well for voltage imbalance and voltage distortion events.

## Appendix
## General Branch Current Expression

For small amounts of imbalance and some simplification, there are tractable symbolic expressions for the branch currents. $I_{12}(s)$ is used to illustrate the result. Expressions for

$I_{23}(s)$ and $I_{31}(s)$ parallel the developed example. The system is analyzed with the following substitution, $V_{ca}(s) = -(V_{ab}(s) - V_{bc}(s))$, and consequently, the terms $H_{13}(s)$, $H_{21}(s)$, and $H_{32}(s)$ are equal to zero. Also, the following simplifications are made; the product of two imbalance capacitances are neglected, for example, $\Delta C_{a1}\Delta C_{a2}$, and products with three capacitances, one of them being an imbalance capacitance, are neglected, for example, $\Delta C_{a1}C_p^2$ or $\Delta C_{a1}C_pC_s$. From (10), $I_{12}(s)$ is

$$I_{12}(s) = H_{11}(s)V_{ab}(s) + H_{12}(s)V_{bc}(s). \tag{20}$$

The terms $H_{11}(s)$ and $H_{12}(s)$ have a common denominator

$$\begin{aligned}\mathrm{den}(H_{11}(s)) = {} & (C_p^3 + 8C_s^3 + 6C_p^2C_s + 12C_pC_s^2)R^2s^2 \\ & + (6C_p^2 + 24C_s^2 + 24C_pC_s)Rs + 9C_p + 18C_s \\ & + ((4C_p + 8C_s)Rs + 3)\sum \Delta C_{xx}\end{aligned} \tag{21}$$

where $\sum \Delta C_{xx}$ is the sum of the imbalance capacitances listed in (11). The numerators of $H_{11}(s)$ and $H_{12}(s)$ are

$$\begin{aligned}&\mathrm{num}(H_{11}(s)) \\ &\quad = s(C_p^3 - 4C_s^3 + 3C_p^2C_s)Rs + 3C_p^2 - 6C_s^2 \\ &\qquad + C_pC_s + C_p(3\Delta C_{a1} - \Delta C_{a2} + \Delta C_{a3} + 2\Delta C_{b2} \\ &\qquad + \Delta C_{b3} + 2\Delta C_{c2} + \Delta C_{c3}) \\ &\qquad + C_s(3\Delta C_{a1} - 5\Delta C_{a2} - \Delta C_{a3} - 3\Delta C_{b1} + \Delta C_{b2} \\ &\qquad - \Delta C_{b3} - 3\Delta C_{c1} + \Delta C_{c2} + \Delta C_{c3}))\end{aligned} \tag{22}$$

$$\begin{aligned}&\mathrm{num}(H_{12}(s)) \\ &\quad = s((C_p + 2C_s)(\Delta C_{a1} - \Delta C_{b2} \\ &\qquad - \Delta C_{a2} + \Delta C_{b1} - 2\Delta C_{c1} + 2\Delta C_{c2})).\end{aligned} \tag{23}$$

If all imbalance capacitances are equal to zero, $H_{12}(s)$ is equal to zero and the expression for $H_{11}(s)$ in (12) is obtained.

## REFERENCES


[1] J. S. Donnal and S. B. Leeb, "Noncontact power meter," *IEEE Sensors J.*, vol. 15, no. 2, pp. 1161–1169, Feb. 2015.

[2] A. J. Thomas, C. Iyyappan, and C. C. Reddy, "A method for surface voltage measurement of an overhead insulated conductor," *IEEE Trans. Instrum. Meas.*, vol. 70, pp. 1–8, 2021.

[3] W. Fang *et al.*, "Noncontact RF voltage sensing of a printed trace via a capacitive-coupled probe," *IEEE Sensor J.*, vol. 18, no. 21, pp. 8873–8882, Nov. 2018.

[4] D. Lawrence, J. S. Donnal, S. Leeb, and Y. He, "Non-contact measurement of line voltage," *IEEE Sensors J.*, vol. 16, no. 24, pp. 8990–8997, Dec. 2016.

[5] M. A. Haberman and E. M. Spinelli, "Noncontact AC voltage measurements: Error and noise analysis," *IEEE Trans. Instrum. Meas.*, vol. 67, no. 8, pp. 1946–1953, Aug. 2018.

[6] M. A. Haberman and E. M. Spinelli, "A noncontact voltage measurement system for power-line voltage waveforms," *IEEE Trans. Instrum. Meas.*, vol. 69, no. 6, pp. 2790–2797, Jun. 2020.

[7] P. S. Shenil and B. George, "Development of a nonintrusive true-RMS AC voltage measurement probe," *IEEE Trans. Instrum. Meas.*, vol. 68, no. 10, pp. 3899–3906, Oct. 2019.

[8] M. Botha, "Wideband modelling of capacitive voltage sensors for open-air transmission line applications," Ph.D. dissertation, Dept. Elect. Electron. Eng., Univ. Stellenbosch, Stellenbosch, South Africa, 2002.

[9] S. V. D. Merwe, "Modelling and performance evaluation of a three-phase capacitive voltage sensor topology," M.S. thesis, Dept. Elect. Electron. Eng., Univ. Stellenbosch, Stellenbosch, South Africa, 2006.

[10] F. Barakou, P. A. A. F. Wouters, S. Mousavi-Gargari, J. P. W. de Jong, and E. F. Steennis, "Online transient measurements of EHV cable system and model validation," *IEEE Trans. Power Del.*, vol. 34, no. 2, pp. 532–541, Apr. 2019.

[11] L. Wu, P. A. A. F. Wouters, E. J. M. van Heesch, and E. F. Steennis, "On-site voltage measurement with capacitive sensors on high voltage systems," in *Proc. IEEE Trondheim PowerTech*, Jun. 2011, pp. 1–6.

[12] *IEEE Guide for the Design and Installation of Cable Systems in Substations*, IEEE Standard 525-2016 (Revision IEEE Standard 525-2007), 2016, pp. 1–243.

[13] W. F. Powers, "The basics of power cable," in *Proc. IEEE 36th Cement Ind. Tech. Conf.*, Apr. 1994, pp. 37–45.

[14] *IEEE Guide for Field Testing and Evaluation of the Insulation of Shielded Power Cable Systems Rated 5 KV and Above—Redline*, IEEE Standard 400-2012 (Revision IEEE Standard 400-2001), 2012, pp. 1–159.

[15] N. O. M. Sadiku, *Elements of Electromagnetics*. Philadelphia, PA, USA: Saunders College Publishing, 1989.

[16] *Symbolic Math Toolbox*, Mathworks, Natick, MA, USA, 2021.

[17] J. J. Cooley, A.-T. Avestruz, and S. B. Leeb, "A retrofit capacitive sensing occupancy detector using fluorescent lamps," *IEEE Trans. Ind. Electron.*, vol. 59, no. 4, pp. 1898–1911, Apr. 2012.

[18] A.-T. Avestruz, J. J. Cooley, D. Vickery, J. Paris, and S. B. Leeb, "Dimmable solid state ballast with integral capacitive occupancy sensor," *IEEE Trans. Ind. Electron.*, vol. 59, no. 4, pp. 1739–1750, Apr. 2012.

[19] P. Lindahl, A.-T. Avestruz, W. Thompson, E. George, B. R. Sennett, and S. B. Leeb, "A transmitter—Receiver system for long-range capacitive sensing applications," *IEEE Trans. Instrum. Meas.*, vol. 65, no. 10, pp. 2412–2423, Oct. 2016.

[20] J. Karki, "Fully-differential amplifiers," Texas Instrum., Dallas, TX, USA, Tech. Rep. SLOAO54E, 2016.

[21] J. Karki, "Input impedance matching with fully differential amplifiers," Texas Instrum., Dallas, TX, USA, Tech. Rep. SLYT310, 2008.

[22] J. J. Cooley, A.-T. Avestruz, and S. B. Leeb, "Small-signal analysis of fully-differential closed-loop op-amp circuits with arbitrary external impedance elements," *IET Circuits Devices Syst.*, vol. 5, no. 5, pp. 371–383, 2011.

[23] *THS4551: Low-Noise, Precision, 150-MHz, Fully Differential Amplifier*, Texas Instrum., Dallas, TX, USA, 2017.

[24] *OPA2377: 5MHz, Low-Noise, Dual, CMOS Operational Amplifiers*, Texas Instrum., Dallas, TX, USA, 2011.

[25] FastFieldSolvers S. R. L. *Electromagnetic Workbench for Freecad*. (2019). [Online]. Available: https://github.com/ediloren/EM-Workbench-for-FreeCAD

[26] FastFieldSolvers S. R. L. *Fastercap*. (2019). [Online]. Available: https://github.com/ediloren/FasterCap

[27] K. Camenzind, "Non-contact voltage monitoring of three-phase power cables," M.S. thesis, Massachusetts Inst. Technol., Cambridge, MA, USA, 2020.

[28] S. R. Shaw, S. B. Leeb, L. K. Norford, and R. W. Cox, "Nonintrusive load monitoring and diagnostics in power systems," *IEEE Trans. Instrum. Meas.*, vol. 57, no. 7, pp. 1445–1454, Jul. 2008.

[29] R. Cox, S. B. Leeb, S. R. Shaw, and L. K. Norford, "Transient event detection for nonintrusive load monitoring and demand-side management using voltage distortion," in *Proc. 21st Annu. IEEE Appl. Power Electron. Conf. Expo.*, Mar. 2006, pp. 1–7.

[30] S. C. Shabshab *et al.*, "Demand smoothing in military microgrids through coordinated direct load control," *IEEE Trans. Smart Grid*, vol. 11, no. 3, pp. 1917–1927, May 2020.

[31] J. Paris, J. S. Donnal, Z. Remscrim, S. B. Leeb, and S. R. Shaw, "The sinefit spectral envelope preprocessor," *IEEE Sensors J.*, vol. 14, no. 12, pp. 4385–4394, Dec. 2014.


**Thomas C. Krause** (Graduate Student Member, IEEE) received the B.S degree in electrical engineering from Purdue University, West Lafayette, IN, USA, in 2019, and the M.S. degree in electrical engineering and computer science from the Massachusetts Institute of Technology, Cambridge, MA, USA, in 2021, where he is currently pursuing the Ph.D. degree in electrical engineering and computer science.

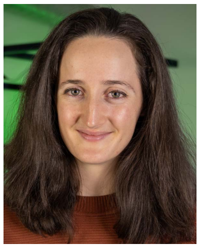

**Katherine Camenzind** received the B.S. and M.Eng. degrees in electrical engineering and computer science from the Massachusetts Institute of Technology, Cambridge, MA, USA, in 2018 and 2020, respectively.

She is currently a Software Engineer on the Hardware Team at Tulip Interfaces, Somerville, MA, USA.

**Daisy H. Green** (Graduate Student Member, IEEE) received the B.S. degree in electrical engineering from the University of Hawai'i at Manoa, Honolulu, HI, USA, in 2015, and the M.S. degree in electrical engineering from the Massachusetts Institute of Technology, Cambridge, MA, USA, in 2018, where she is currently pursuing the Ph.D. degree.

**Andrew Moeller** is currently pursuing the M.S. degree in naval architecture and marine engineering with the Massachusetts Institute of Technology, Cambridge, MA, USA.

He previously served as the Damage Control Assistant on USCGC JAMES (WMSL 754) and as the Executive Officer on USCGC THUNDER BAY (WTGB 108). He is a Lieutenant with the United States Coast Guard.

**Łukasz Huchel** received the B.Sc. degree in electrical power engineering from the Silesian University of Technology, Gliwice, Poland, in 2013, the M.Sc. degree from the Department of Electrical Engineering and Computer Science (EECS), Masdar Institute of Science and Technology, Abu Dhabi, United Arab Emirates, in 2015, and the Ph.D. degree from the Massachusetts Institute of Technology, Cambridge, MA, USA, in 2021.

He is currently with Enphase Energy, Austin, TX, USA.

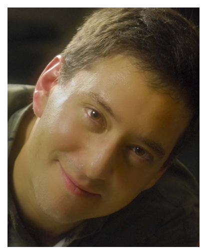

**Steven B. Leeb** (Fellow, IEEE) received the Ph.D. degree from the Massachusetts Institute of Technology (MIT), Cambridge, MA, USA, in 1993.

He has served as a Commissioned Officer at the USAF reserves and he has been a member of the MIT faculty at the Department of Electrical Engineering and Computer Science since 1993. He also holds a joint appointment at the Department of Mechanical Engineering, MIT. He is the author or coauthor of over 200 publications and 20 U.S. patents in the fields of electromechanics and power electronics.